nature communications

Article

https://doi.org/10.1038/s41467-024-54972-x

Portable, low-field magnetic resonance imaging for evaluation of Alzheimer's disease

Received: 1 June 2024

Accepted: 21 November 2024

Published online: 02 December 2024

Check for updates

Annabel J. Sorby-Adams[1,2], Jennifer Guo[1,2], Pablo Laso[3], John E. Kirsch[3], Julia Zabinska[4], Ana-Lucia Garcia Guarniz[1], Pamela W. Schaefer[5], Seyedmehdi Payabvash[6], Adam de Havenon[4], Matthew S. Rosen[3], Kevin N. Sheth[4], Teresa Gomez-Isla[1], J. Eugenio Iglesias[3] & W. Taylor Kimberly[1,2]

Portable, low-field magnetic resonance imaging (LF-MRI) of the brain may facilitate point-of-care assessment of patients with Alzheimer's disease (AD) in settings where conventional MRI cannot. However, image quality is limited by a lower signal-to-noise ratio. Here, we optimize LF-MRI acquisition and develop a freely available machine learning pipeline to quantify brain morphometry and white matter hyperintensities (WMH). We validate the pipeline and apply it to outpatients presenting with mild cognitive impairment or dementia due to AD. We find hippocampal volumes from ≤ 3 mm isotropic LF-MRI scans have agreement with conventional MRI and are more accurate than anisotropic counterparts. We also show WMH volume has agreement between manual segmentation and the automated pipeline. The increased availability and reduced cost of LF-MRI, in combination with our machine learning pipeline, has the potential to increase access to neuroimaging for dementia.

Alzheimer's disease (AD) is characterized by the pathological deposition of amyloid-β (Aβ) and formation of neurofibrillary tangles in the brain[1]. The progressive accumulation of these proteins lead to degenerative changes in brain structure and frequently coincide with vascular injury, characterized by brain atrophy and white matter hyperintensities (WMH), respectively. A burgeoning aging population and accumulating risk factors is leading to an increased lifetime risk of dementia, with prevalence predicted to reach 139 million worldwide by the year 2050[2]. Patients with AD have a progressive pre-symptomatic stage lasting 10–20 years, with individuals often receiving a diagnosis after cognitive impairment is already well established. Consequently, an estimated 75% of people with dementia remain undiagnosed globally, with rates as high as 90% in low and middle income countries[3]. The advent of anti-amyloid therapies has highlighted the importance of identifying individuals with mild cognitive impairment (MCI) or AD who may benefit from treatment, and their subsequent monitoring for both disease progression and treatment side effects.

Current AD diagnosis involves cognitive testing, assessment of Aβ and phosphorylated tau burden through positron emission tomography (PET) or fluid biomarkers, and magnetic resonance imaging (MRI)[4]. Multiparametric MRI facilitates assessment of changes in brain structure and integrity, including generalized and hippocampal atrophy[5–7] and accompanying white matter disease[8,9], which accrue over the course of disease progression and precede onset of cognitive decline[10,11]. These features highlight the importance of neuroimaging for the clinical diagnosis and management of MCI and AD, yet there are disparities in access to neuroimaging technologies both locally and globally.

[1]Department of Neurology, Massachusetts General Hospital and Harvard Medical School, Boston, MA, USA. [2]Center for Genomic Medicine, Massachusetts General Hospital, Boston, MA, USA. [3]Athinoula A. Martinos Center for Biomedical Imaging, Massachusetts General Hospital and Harvard Medical School, Boston, MA, USA. [4]Department of Neurology, Center for Brain & Mind Health, Yale New Haven Hospital and Yale School of Medicine, New Haven, CT, USA. [5]Division of Neuroradiology, Department of Radiology, Massachusetts General Hospital and Harvard Medical School, Boston, MA, USA. [6]Division of Neuroradiology, Department of Radiology and Biomedical Imaging, Yale New Haven Hospital and Yale University School of Medicine, New Haven, CT, USA. e-mail: wtkimberly@mgh.harvard.edu

Portable, low-field MRI (LF-MRI) is an emerging neuroimaging technology that has the potential to address some of the barriers intrinsic to MRI on conventional systems operating at 1.5 to 3 Tesla (T)[12,13]. Previous work has demonstrated that LF-MRI is safe, feasible, less costly, and can facilitate point-of-care scanning for acute neurologic conditions[14–16]. The lower power requirements, reduced fringe field, and electromagnetic interference cancellation enable imaging outside of a conventional MRI suite[12]. However, the inherently lower magnetic field strength reduces signal-to-noise ratio (SNR) and thus influences image resolution. To overcome these limitations and explore the potential of LF-MRI for tracking disease correlates in AD patients, we developed machine learning tools to automatically quantify brain morphometry and white matter lesions, and demonstrate the utility of LF-MRI for monitoring of patients with MCI and AD.

To first establish an imaging pipeline for quantifying brain volumes, we iteratively optimized our joint super-resolution and contrast synthesis technique (LF-SynthSR)[17–19] to enhance the resolution of LF images for subsequent segmentation (SynthSeg)[20] and determined the optimal LF acquisition parameters for accurate quantification. We subsequently expanded functionality to enable the measurement of WMH burden (WMH-SynthSeg) through automated segmentation of WMH lesions from T2 fluid attenuated inversion recovery (FLAIR) images acquired at LF. We validated these freely available tools (LF-SynthSR, SynthSeg, and WMH-SynthSeg) using multiple patient cohorts, including a prospective cohort of patients with a diagnosis of MCI or AD.

Results

Automated morphometry

LF-MRI images lack the necessary resolution for automatic segmentation with high-field software analysis tools, but can succeed when first super-resolved (SR) to 1 mm isotropic T1-weighted (T1w) magnetization-prepared rapid gradient-echo (MP-RAGE)-like images[17]. However, our prior super-resolution pipeline (LF-SynthSR, v1) required inputs of both T1w and T2-weighted (T2w) LF-MR images to generate a T1w MP-RAGE-like output. The necessity to co-register low resolution images can lead to co-registration errors and misalignment, decreasing the accuracy of the SR image output and subsequent segmentation. Following an approach we used in other applications[19], we modified LF-SynthSR (v2) to accommodate single image inputs of any tissue contrast (including T1w and T2w), any resolution, and any orientation (Fig. 1a), followed by SynthSeg-derived segmentation (Fig. 1b)[21].

Using this pipeline, we first evaluated the accuracy of automated segmentation in a group of healthy volunteers (cohort 1, N = 20; Supplementary information, Table S1) by comparing AD relevant segmentation volumes (hippocampus, lateral ventricle, and whole brain[22,23]) generated from the original LF-SynthSR (v1; T1w and T2w input images co-registered) and LF-SynthSR v2 (T1w or T2w input separately) against conventional, ground truth high-field (HF) MRI acquired at 3 T (Fig. 1c–h). We examined agreement in volume [e.g., correlation and absolute symmetrized percent difference (ASPD)] and also the degree of spatial overlap (e.g., Dice similarity coefficient).

The correlation of hippocampal volumes between 1 mm MP-RAGE HF-MRI images and co-registered T1/T2w LF-MRI counterparts for LF-SynthSR v1 was $r = 0.70$ (95% confidence interval (CI) 0.53–0.86). However, when the updated version LF-SynthSR v2 was used on T1w images alone, the correlation increased to $r = 0.89$ (95% CI 0.80–0.99; Supplementary information, Table S2). Using the ASPD as an additional measure of accuracy, the hippocampal volume using LF-SynthSR v1 had an ASPD of 7.1% (interquartile range (IQR) 1.1–12.3%) relative to ground truth. In contrast, LF-SynthSR v2 generated hippocampal volumes with an ASPD of 3.3% (IQR 1.8–7.2%, $p = 0.028$) when using T1w images as the input and 2.3% (IQR 0.5–4.4%, $p = 0.015$) when using T2w images (Fig. 1c). Lateral ventricle volume accuracy improved when LF-SynthSR v2 was used as compared with LF-SynthSR v1 (Fig. 1d, both $p < 0.001$), as did the whole brain for the T1w image input (Fig. 1e; $p < 0.001$). Analysis based on correlations relative to ground truth were also similar or improved using LF-SynthSR v2 (Supplementary information, Table S2). As a measure of spatial overlap of the segmented brain volumes of interest, Dice similarity coefficients derived from LF-SynthSR v2 were improved for the hippocampus (Fig. 1f; $p < 0.05$), similar for the lateral ventricles (Fig. 1g), although slightly less accurate for whole brain LF-SynthSR v2 (Fig. 1h).

Voxel size and geometry influence the accuracy of brain morphometry, particularly in the low SNR regime of LF-MRI[24]. Compared to ground truth 1 mm MP-RAGE at 3 T (Fig. 2a), we next systematically varied the image acquisition resolution of T1w (Fig. 2b) and T2w (Fig. 2c) LF-MRI scans, followed by analysis using the LF-SynthSR v2 and SynthSeg pipeline. The image acquisition duration ranged between 1:53 min:sec to 9:48 min:sec depending on sequence, voxel size, and geometry (Supplementary information, Table S3). For the hippocampus, the ASPD difference in volume relative to ground truth was < 5% for all resolutions and comparable across LF T1w and T2w contrasts (Supplementary information, Fig. S1). Correlation between hippocampal, whole brain, and lateral ventricle volumes derived at LF and HF were comparable among T1w and T2w contrasts when the voxel dimensions were isotropic and ≤ 3 mm (Supplementary information, Table S4). Furthermore, Dice similarity coefficients demonstrated optimal spatial overlap between HF and LF counterparts when the voxel sizes were isotropic and ≤ 3 mm ($p < 0.01$, Fig. 3a, b) which was observed irrespective of co-registration direction (see Supplementary information, Table S5). Re-scanning of participants in a separate session demonstrated high test-retest agreement, where isotropic 3 mm acquisition also had improved Dice similarity coefficients compared with anisotropic counterparts ($p < 0.05$, Fig. 3c). Similar results were obtained for lateral ventricle (Fig. 3d–f) and whole brain (Fig. 3g–i) volumes across the range of tissue contrasts and voxel sizes (see also Supplementary information, Table S4). Finally, we validated our LF-SynthSR v2 segmentation pipeline against HF T1w MP-RAGE segmentations derived from the well-established FreeSurfer segmentation tool ASEG[25], which revealed hippocampal correlations of $r > 0.83$, ASPD < 6.5% and Dice coefficients > 0.80 for all T1w image inputs, and correlations of $r > 0.81$, ASPD < 8.3% and Dice > 0.81 for T2w images across all voxel dimensions (Supplementary information Table S6). Similar results for lateral ventricle and whole brain are also shown (Supplementary information Table S6).

Automated WMH quantification

A common pathologic finding among patients with cognitive impairment is the presence of WMH lesions, which may be due to cerebral small vessel disease or axonal loss[26]. These imaging findings manifest on FLAIR as T2 hyperintense lesions, and automated quantification of these lesions would expand LF-MRI capability for AD diagnosis and monitoring. However, automated T2 lesion segmentation pipelines designed for conventional 1.5–3 T MRI are unable to identify and segment lesions on LF images[21]. Therefore, we next sought to implement a machine learning algorithm to generate WMH lesion volumes (WMHv) from LF-FLAIR images using WMH-SynthSeg[21]. We designed this to simultaneously enable segmentation of WMH T2 FLAIR lesions in addition to the prior brain morphometry.

To first assess the accuracy of WMH segmentation, we analyzed a cohort of aged individuals with WMH lesions and concomitant vascular risk factors (cohort 2, N = 23; Supplementary information Table S7) that had paired LF- and HF-FLAIR images[27], an example of which is shown in Fig. 4a (blue mask and 3D render). First, we compared the volume of WMH lesions on LF-FLAIR using WMH-SynthSeg relative to the paired HF-FLAIR images, which showed a correlation of $r = 0.92$ ($p < 0.001$, Fig. 4b). The WMHv generated by WMH-SynthSeg was also correlated with the respective manually outlined WMH lesions

https://doi.org/10.1038/s41467-024-54972-x

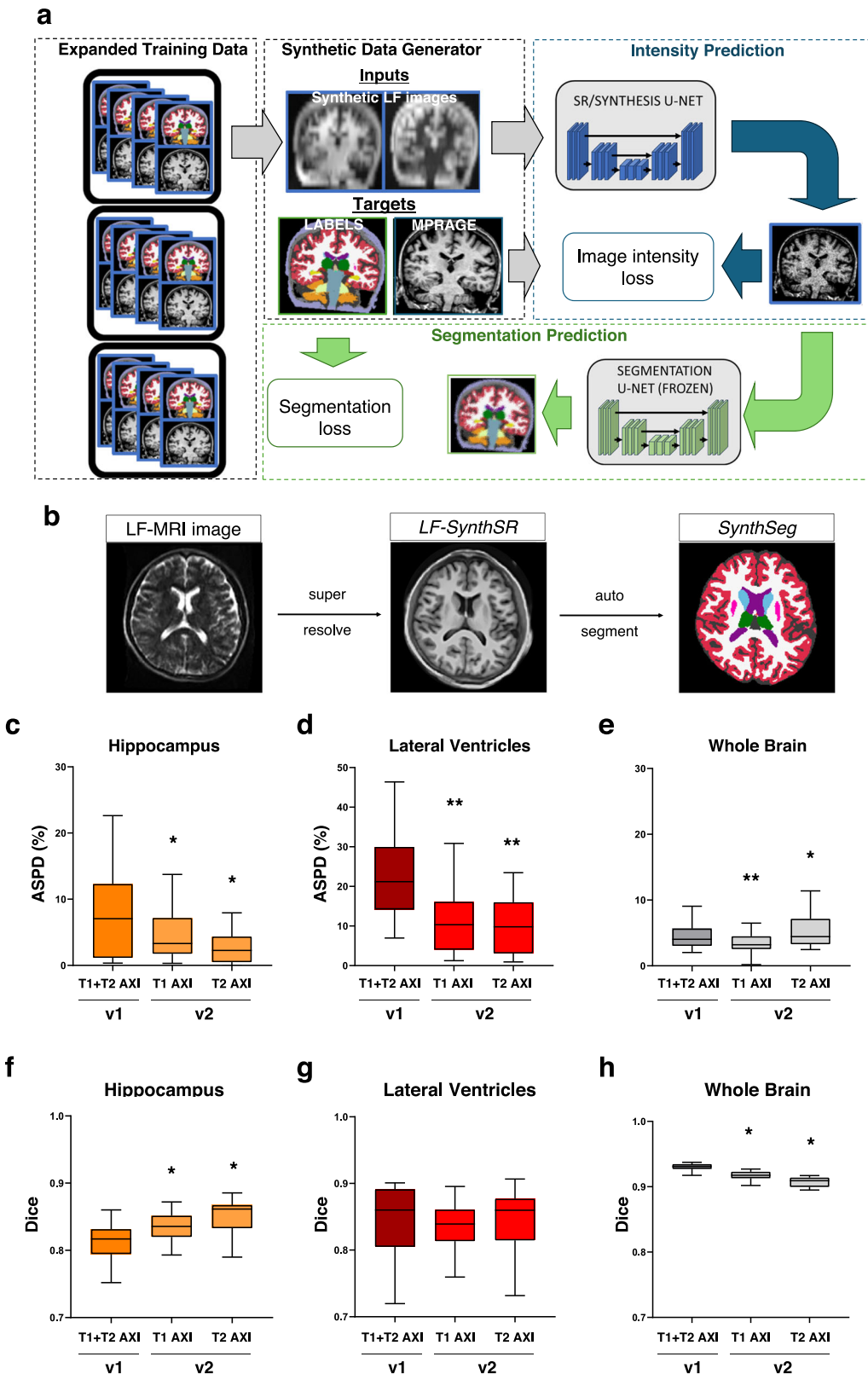

at HF and LF (HF-FLAIR, $r = 0.84$, $p < 0.001$; and LF-FLAIR, $r = 0.81$, $p < 0.001$; Figs. 4c, d, respectively). The visually graded Fazekas scale is frequently used to categorize WMH accrual[28]. We found that WMHv generated by WMH-SynthSeg showed a stepwise increase relative to the periventricular Fazekas score (Fig. 4e, $p = 0.022$), the deep white matter Fazekas score (Fig. 4f, $p = 0.003$), and a dichotomized composite score (Fig. 4g, $p = 0.004$).

Application to MCI/AD patients

We next prospectively studied a cohort of patients who presented to the Memory Disorders outpatient neurology clinic with a diagnosis of MCI or dementia due to AD (cohort 3, N = 54; Supplementary information Table S8). We applied the imaging analysis pipelines LF-SynthSR v2 and SynthSeg to derive hippocampal, whole brain, and lateral ventricle volumes and WMH-SynthSeg to quantify WMHv at LF

https://doi.org/10.1038/s41467-024-54972-x

Fig. 1 | Fine-tuning of LF-SynthSR and overall imaging analysis pipeline and performance. a The architecture of the convolutional neural network LF-SynthSR (v2). **b** The overall imaging analysis pipeline includes acquisition of LF-MRI images at different contrasts and resolutions, super-resolving the raw images with LF-SynthSR followed by segmentation using SynthSeg. **c**–**h** LF-MRI images were prepared with the original (v1, T1 + T2 AXI) or fine-tuned (v2, T1 and T2 AXI) LF-SynthSR followed by automated segmentation with SynthSeg. LF-MRI segmentation volumes for the hippocampus (**c** and **f**), lateral ventricles (**d** and **g**) and whole brain (**e** and **h**) were compared with volumes derived from 1 mm MP-RAGE images acquired at high-field using the absolute symmetrized percentage difference (ASPD) and Dice coefficient. The ASPD for hippocampus (T1w $p = 0.027$; T2w $p = 0.014$) and lateral ventricle volumes ($p < 0.001$ for T1w and T2w) relative to high-field was less for T1w or T2w LF-MRI inputs when LF-SynthSR v2 was used. The ASPD for whole brain was improved for T1w ($p < 0.001$) but not for T2w ($p = 0.040$) when using LF-SynthSR v2. The Dice coefficient for the hippocampus was more accurate when v2 was used for both T1w ($p = 0.022$) and T2w inputs ($p < 0.001$), similar for lateral ventricles, and lower for the whole brain ($p < 0.001$). For each subpanel, the box plots show the median, the interquartile range, and the Tukey whiskers. Each box plot corresponds to $n = 20$ biological replicates. Source data is available via the following link: https://doi.org/10.7910/DVN/9PANMC. AXI, axial; LF, low-field; T1w, T1 weighted; T2w, T2 weighted. * $p < 0.05$, ** $p < 0.01$ using the Wilcoxon signed rank test compared to v1.

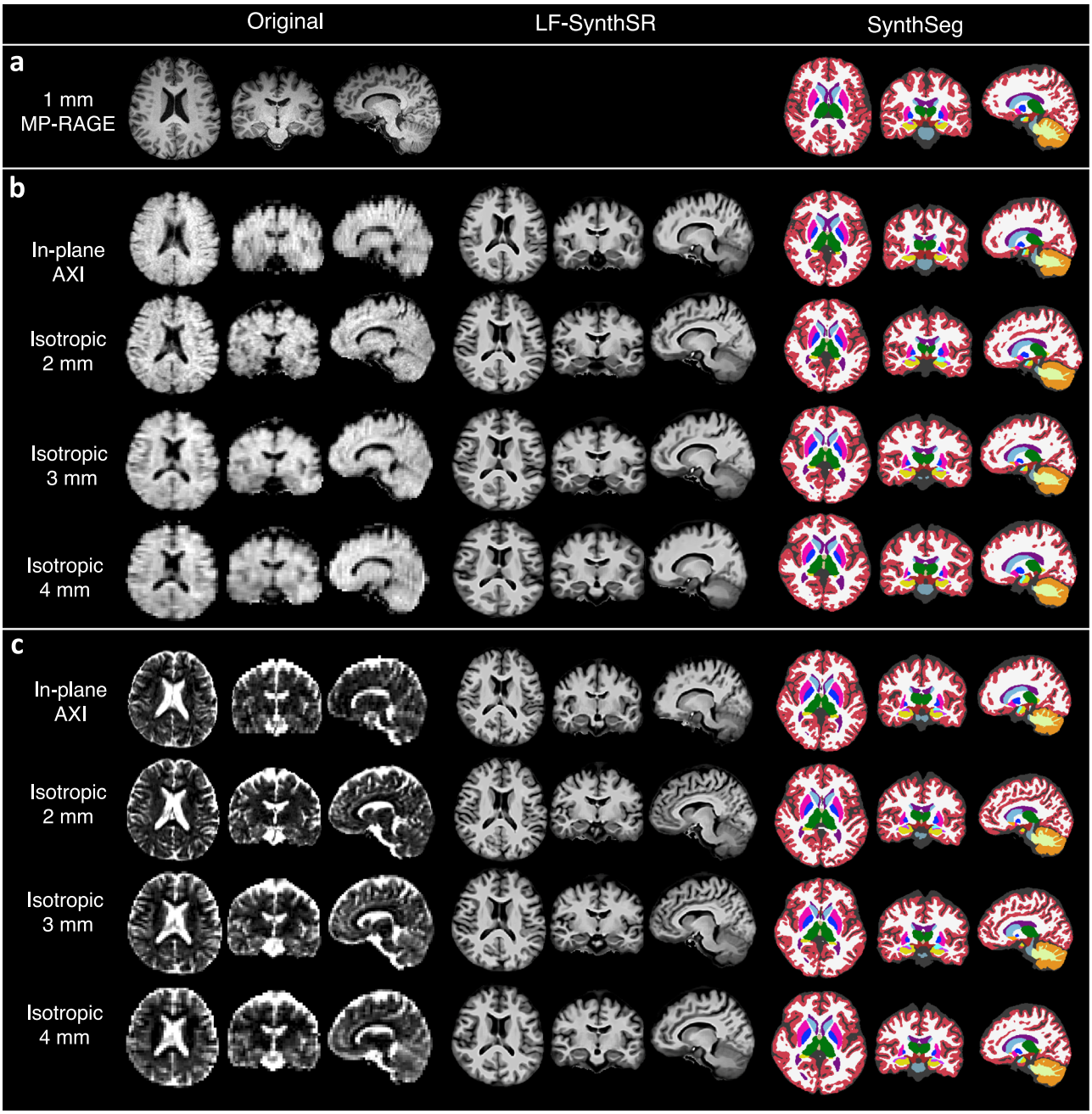

Fig. 2 | Axial, sagittal, and coronal views of original and processed images at different resolutions from one healthy volunteer subject. a Isotropic 1 mm MP-RAGE images acquired at 3 T are shown, including ground truth SynthSeg segmentation. **b** T1w and **c** T2w images acquired at anisotropic (AXI) and varying isotropic voxel sizes at LF were super-resolved with LF-SynthSR (v2) and automatically segmented by SynthSeg. MP-RAGE, Magnetization Prepared-RApid Gradient Echo; AXI, axial.

https://doi.org/10.1038/s41467-024-54972-x

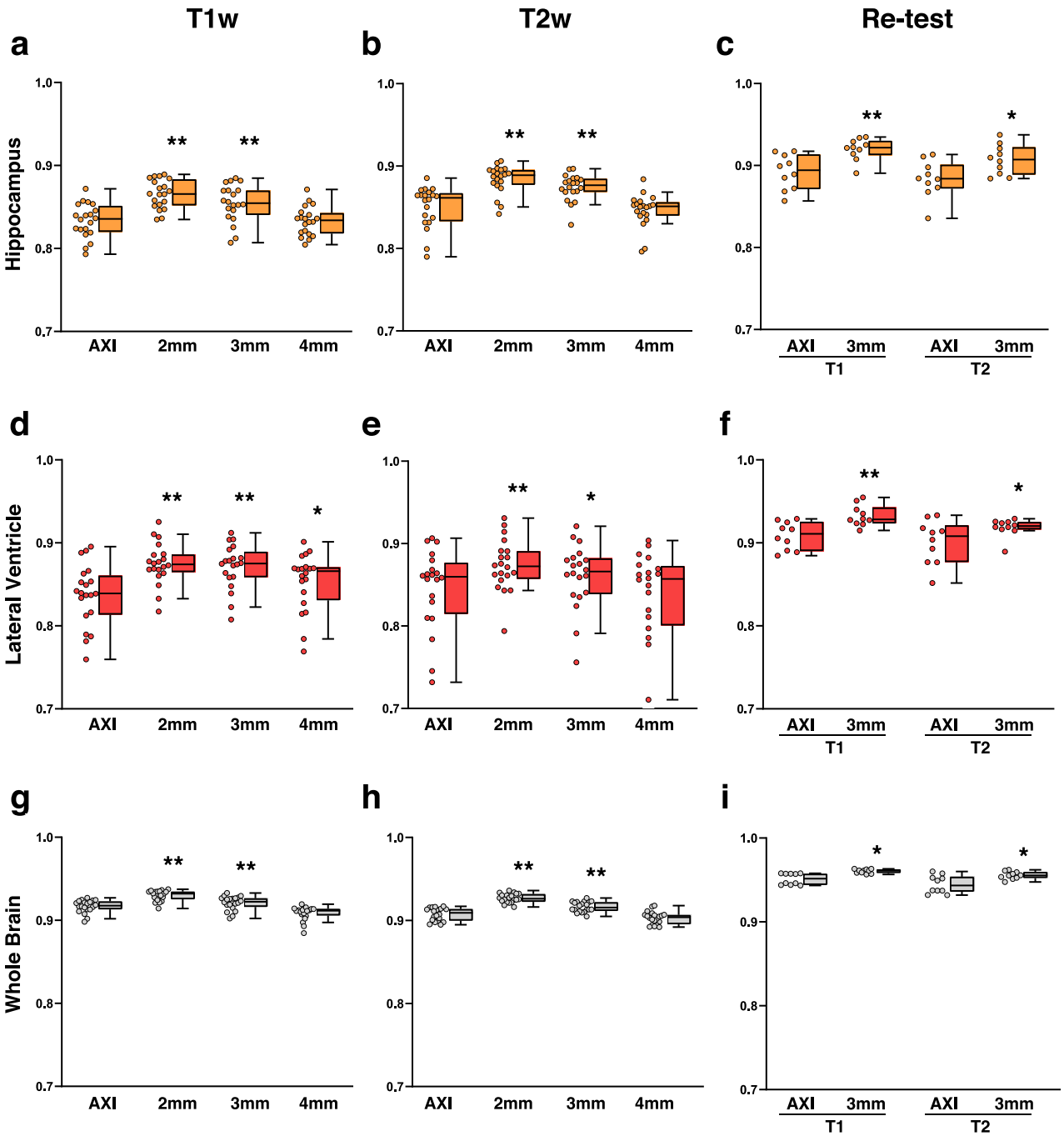

Fig. 3 | Accuracy of brain volumes varies as a function of the initial image acquisition resolution at LF. a The Dice similarity coefficient of the hippocampus derived from LF T1w images of anisotropic (T1 AXI) or varying isotropic resolutions was compared to 1 mm MP-RAGE images acquired at 3 T. Dice scores were higher when isotropic voxels ≤ 3 mm were used ($p < 0.001$) and (**b**) similar accuracy was obtained from T2w images ($p < 0.001$ for voxels ≤ 3 mm). **c** Re-scanning demonstrates higher test-retest agreement in 3.0 mm isotropic relative to anisotropic counterparts (T1w, $p = 0.0059$; T2w, $p = 0.014$). Similar improvements in the Dice coefficient were observed for voxel sizes ≤ 3.0 mm for the lateral ventricle volume and whole brain using (**d**) and (**g**) T1w images, **e** and **h** T2w images and (**f**) and (**i**) test-retest analysis, respectively. For each subpanel, the box plots show the median, the interquartile range, and the Tukey whiskers and the individual data points are shown adjacent to the box plots. The Wilcoxon signed rank test was used for analysis for $n = 20$ biological replicates, except for the test-retest analysis where $n = 10$. Source data is available via the following link: https://doi.org/10.7910/DVN/9PANMC. T1w, T1 weighted; T2w, T2 weighted; AXI, axial. * $p < 0.05$, ** $p < 0.01$ for all panels.

relative to clinically acquired 1.5–3 T MRI (case example, Fig. 5a) and determined the accuracy of these pipelines between LF and HF counterparts and their relevance to differential disease states.

Hippocampal volumes derived from LF- and HF- MRI counterparts were in close agreement (ASPD 2.8%, IQR 1.9–7.3%), revealing a correlation of $r = 0.85$ (95% CI 0.77–0.93, $p < 0.001$; Fig. 5b) and a Dice similarity coefficient of 0.87 (95% CI 0.85–0.88). Similar results were obtained when examining lateral ventricle and whole brain volumes (Fig. 5b; $r = 0.99$; 95% CI 0.98–0.99; and $r = 0.97$; 95% CI 0.95–0.98, respectively; $p < 0.001$; see Supplementary information Table S9 for ASPD and Dice similarity coefficients). Test-retest analysis revealed an ASPD < 4.0%, DICE coefficient > 0.9 and correlation $r > 0.8$ for hippocampal, lateral ventricle and whole brain volumes (see Supplementary information Table S10). WMHv derived from LF-FLAIR were also

https://doi.org/10.1038/s41467-024-54972-x

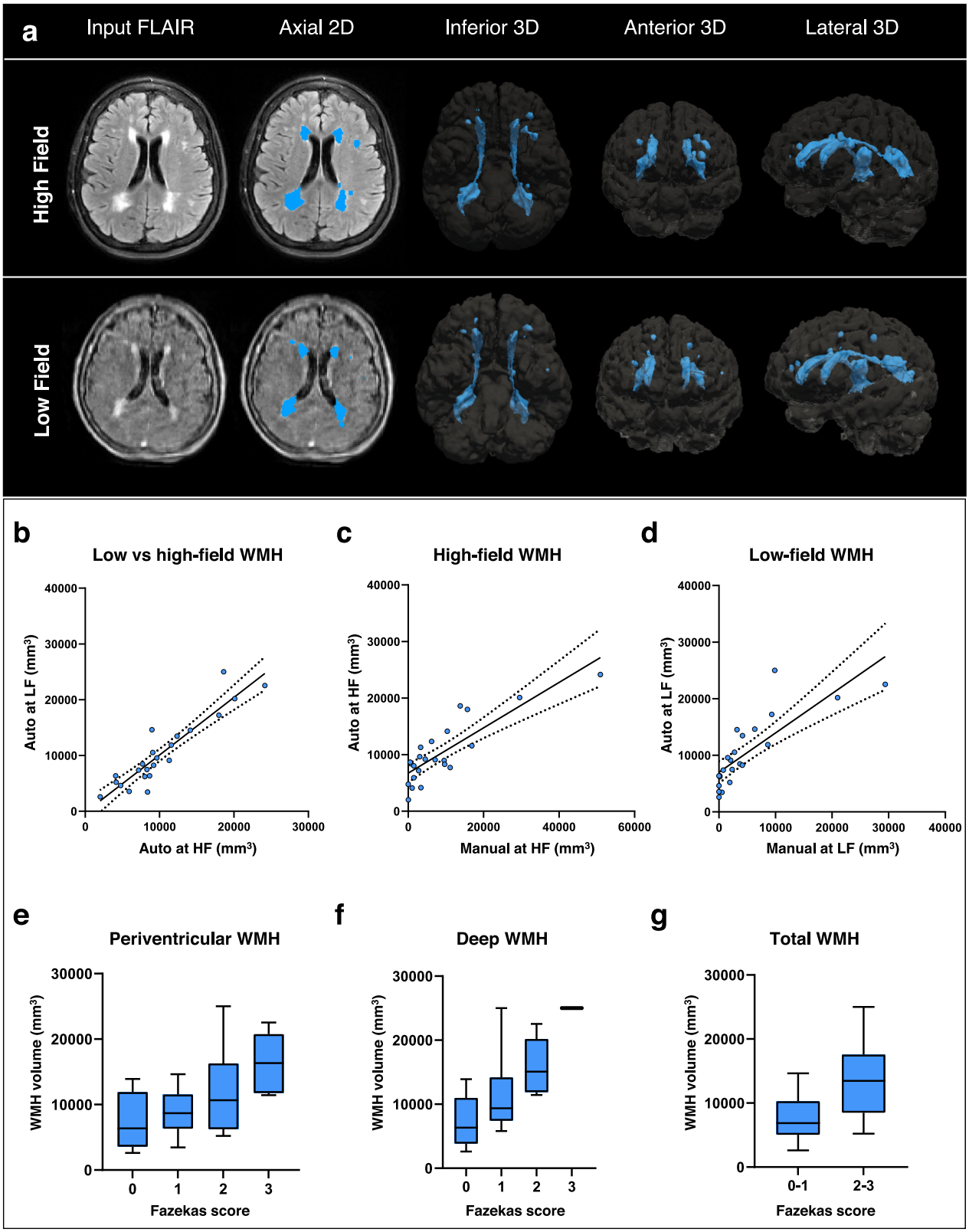

Fig. 4 | WMH-SynthSeg can automatically segment WMH on LF-MRI FLAIR sequences in patients presenting without neurologic complaints yet concomitant vascular risk factors. a An example of a subject with WMH at HF- and LF-MRI, with automatically segmented lesions outlined (blue) in the axial plane and with 3D rendering. **b**) WMH volume scatterplot and linear fit of WMH volumes derived at LF- compared to HF-MRI using WMH-SynthSeg ($r = 0.91$, $p < 0.001$). **c** Scatterplot of WMH volumes derived from automatic segmentation versus manual outlining at HF, and similarly at LF in (**d**). WMH volume ($n = 23$) was associated with the periventricular Fazekas score (**e**), the deep Fazekas score in (**f**), and the composite Fazekas score in (**g**). For each subpanel, the box plots shows the median, the interquartile range, and the Tukey whiskers. Source data is available via the following link: https://doi.org/10.7910/DVN/9PANMC. WMH, white matter hyperintensity volume; LF, low-field; HF, high-field.

https://doi.org/10.1038/s41467-024-54972-x

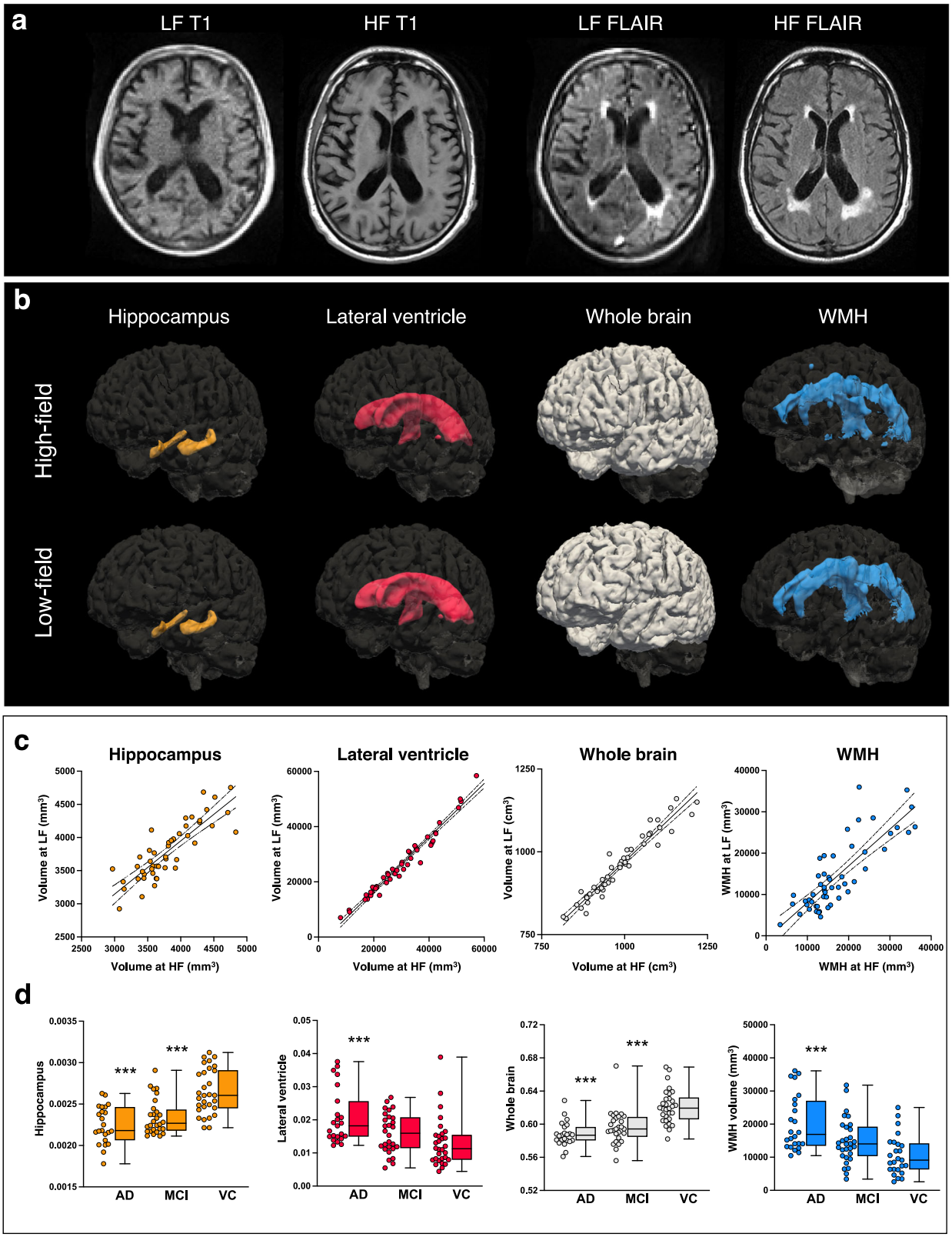

correlated with volumes from HF-FLAIR ($r = 0.82$, 95% CI 0.74–0.91, $p < 0.001$; Fig. 5b, righthand most panel).

We next determined if our machine learning pipelines could accurately differentiate between patients with a diagnosis of MCI or AD and those who are cognitively normal (CN). As an initial validation step, we first assessed 1.5 T MRI scans derived from CN, MCI and AD patients in the established Alzheimer's Disease Neuroimaging Initiative (ADNI) cohorts (N = 61; Supplementary information Table S11). Consistent with previously reported results, we verified that MCI and AD ADNI subjects had smaller hippocampal volumes than CN subjects when analyzed with our pipeline ($p = 0.002$ and $p < 0.001$, respectively), although lateral ventricle and whole brain volumes were similar among these groups ($p = 0.13$ and $p = 0.44$, respectively). We subsequently validated the WMHv generated by WMH-SynthSeg with previously

Fig. 5 | Application of LF-SynthSR v2 and WMH-SynthSeg to a cohort of MCI/AD subjects imaged in the clinic at LF. a Representative T1 weighted (T1w) and FLAIR images at low field (LF) and high field (HF) in a patient with Alzheimer's disease (AD). T1w images are processed through LF-SynthSR v2 (LF) and SynthSeg and FLAIR images are processed through WMH-SynthSeg. **b** Hippocampal (orange), lateral ventricle (red) and whole brain (light gray) volumes derived from SynthSeg and WMH (blue) derived from WMH-SynthSeg are shown in the 3D rendering for LF and HF counterparts. **c** Scatter plots comparing the hippocampus, lateral ventricle, whole brain, and WMH volume derived from HF-MRI and LF-MRI scans are shown. **d** Using LF-MRI scans, the hippocampus and whole brain volumes were smaller among Alzheimer's disease (AD, $n = 24$) and mild cognitive impairment (MCI; $n = 30$) patients compared to the vascular cohort (VC; $n = 23$) presenting without memory complaints, and patients with AD had larger ventricles. Patients with AD also had greater WMH burden compared with the VC. Segmentation volumes are adjusted for total intracranial volume in mm^3. For each subpanel, the box plots show the median, the interquartile range, and the Tukey whiskers. The individual data points are shown adjacent to the box plots. Source data is available via the following link: https://doi.org/10.7910/DVN/9PANMC. WMH, white matter hyperintensity. *** $p < 0.001$, compared to the VC.

derived volumes measured on ADNI HF-FLAIR scans (N = 58; Supplementary information Table S12), and revealed a correlation in WMHv of $r = 0.91$ (95% CI 0.83–0.99, $p < 0.001$).

Finally, we assessed whether our pipeline could distinguish MCI and AD from non-AD subjects exclusively using LF-MRI. Patients with a diagnosis of MCI or AD demonstrated smaller hippocampal and whole brain volumes when compared to the vascular cohort, and patients with AD had larger lateral ventricles (all $p < 0.001$, Fig. 5d). Automatically quantified WMHv burden was also greater in those with AD compared to those without memory complaints ($p < 0.001$, Fig. 5d), and WMHv demonstrated a stepwise relationship with qualitative Fazekas scores among MCI and AD patients ($p < 0.001$). A subset of MCI and AD patients had cerebrospinal fluid (CSF) Aβ biomarkers obtained for their clinical care ($n = 21$). In these patients, a lower level of CSF $A\beta_{42}$, which decreases as a consequence of Aβ aggregation in the brain and is thus used as a marker of disease progression[29,30], correlated with larger ventricle volumes derived from LF-MRI ($r = -0.46$, 95% CI −0.75 – −0.02, $p = 0.038$). Lower CSF $A\beta_{42}$ was also associated with a higher burden of deep WMH ($r = -0.63$, 95% CI −0.84 – −0.26, $p = 0.002$) but not total WMH burden.

Discussion

In this study, we present an end-to-end LF-MRI acquisition pipeline that automatically quantifies brain and WMH volumes with comparable accuracy to HF-MRI. To validate machine learning tools for automated quantification, we demonstrated that brain volumes segmented from ≤ 3 mm isotropic LF-MRI images were more accurate than anisotropic counterparts, and that white matter lesions segmented using automated tools have strong agreement with those segmented manually. We applied this pipeline to patients with MCI/AD and demonstrate a similar pattern of brain atrophy and WMH to that observed on conventional MRI, with strong agreement between brain morphometry and WMH volumes generated via automated and manual counterparts, and an ability to leverage these LF-MRI pipelines to distinguish between non-AD patients and those with a diagnosis of MCI/AD.

Given its portability and low operational cost, LF-MRI holds promise as a tool to complement and extend access to current approaches for AD diagnosis, monitoring and management. Atrophy is an established biomarker for AD, with effects primarily observed in the hippocampus, whole brain, and ventricles[31,32], with structural changes observed on MRI often preceding cognitive impairment in the order of years. Hippocampal atrophy is present in pre-symptomatic individuals who subsequently develop AD, with hippocampal volumes reduced by 15–25% among MCI and mild AD compared to cognitively normal individuals, and with rates of hippocampal atrophy of 3–5% per year[33–38]. Ventricular enlargement also has demonstrated sensitivity to disease progression, as patients with MCI who convert to AD have a higher rate of ventricular enlargement compared to those with stable MCI[39]. Our findings indicate that LF-MRI can detect hippocampal, lateral ventricle, and whole brain volumes with strong agreement to ground truth and high test-retest reliability. Moreover, we show that volumes acquired from LF-MRI follow a similar pattern to that observed on conventional MRI, with less atrophy observed in CN individuals compared to individuals with MCI and AD. These results suggest that LF-MRI has the potential to provide brain volumetric information to monitor AD progression.

Loss of white matter integrity that manifests as WMH lesions is also associated with an increased risk of cognitive impairment[40,41]. Variability in both the pattern and degree of WMH reflects differences in etiology, pathological severity, and subsequent clinical manifestation. Although WMH is prevalent in 20–50% of individuals by midlife, prevalence increases to > 90% with advancing age[42]. WMH has been shown to be associated with elevated cerebral Aβ in the setting of AD, with evidence to suggest cerebral small vessel disease exacerbates the accumulation of Aβ due to impaired perivascular clearance[43]. Evaluating WMH burden is thus of clinical value in distinguishing the impact of vascular contributions to subsequent cognitive decline. In our study, automated segmentation of WMH at LF showed strong correlation to quantitative HF measures and qualitative Fazekas scoring. This pipeline was accurate among multiple cohorts, including those with vascular risk factors and individuals with MCI and AD, indicating its generalizability for quantifying WMH volume.

Our study demonstrates that pairing LF-MRI with an end-to-end machine learning pipeline enables point-of-care scanning and automatic quantification of brain morphometry and WMH volume. The use of portable low-field MRI at the point-of-care in combination with machine learning tools may have future application to disease states including vascular dementia, neurodegenerative tauopathies and synucleinopathies, and in longitudinal analyzes. The pipelines reported herein and related tools[44,45] warrant further evaluation in other low-field MRI scanners as they become available[13,46–50], and may benefit from diagnostic specificity and sensitivity analyzes from expert readers, with particular attention to the detection limit for small pathologic lesions. These represent valuable next steps for future research. Moreover, additional logistical steps will need to be undertaken to promote widespread adoption for clinical use. For example, clinical implementation of the proposed pipeline would require capital investment, training of personnel to operate the scanners, and regulatory clearance of machine learning algorithms. Nevertheless, due to the portability and low operational costs, LF-MRI has substantial potential to increase access and reduce burdens associated with neuroimaging, which may be particularly advantageous in environments where availability of conventional MRI is limited.

Methods

Study Design and Imaging Acquisition Parameters

This study included participants from three cohorts who underwent MRI acquisition on a portable, low-field 0.064 T MRI (Hyperfine Inc.) with a high-field, conventional scan at a field strength of 1.5–3 T. For all cohorts, we deem the 1.5–3 T MRI as the gold standard and thus ground truth. Demographics of each cohort is provided in Supplementary information Tables. LF imaging parameters are provided in Supplementary information Table S3.

Cohort 1 included N = 20 healthy volunteers ($n = 10$ males and $n = 10$ females) with no past medical history of neurological disease or memory complaints (Supplementary information Table S1) imaged at

the Massachusetts General Hospital (MGH) between December 2022 and July 2023. Equal numbers of male and female participants underwent LF-MRI acquisition using T1w, T2w and FLAIR anisotropic, in-plane sequences. To optimize the acquisition parameters that maintained accuracy in segmentation tasks while minimizing acquisition time, we studied the impact of image resolution. To that end, we custom-built isotropic sequences at resolutions of 2, 3, and 4 mm voxel sizes, which were acquired in T1w and T2w contrasts (see Supplementary information Table S3 for imaging parameters and acquisition duration). Ground truth 1 mm isotropic T1 MP-RAGE sequences were acquired at 3 T using a Siemens Prisma MRI scanner.

Cohort 2 included N = 23 patients (n = 11 males and n = 12 females) with at least one vascular risk factor who presented to Yale New Haven Hospital between December 2021 and July 2022 with non-neurologic complaints and no prior history of memory disorder (Supplementary information Table S7). All subjects had a T2 FLAIR sequence acquired using both LF- and HF-MRI. Details on this cohort have been published previously[27], and in the current study we focused on the subset that had a paired HF-MRI FLAIR in addition to a LF-FLAIR image.

Cohort 3 included patients who were evaluated in the MGH outpatient Memory Disorders clinic (N = 54; n = 32 males and n = 22 females; Supplementary information Table S8) with a diagnosis of MCI or AD. Subjects aged ≥60 years old with a clinical diagnosis of MCI or AD who presented to the MGH Memory Disorders clinic between February 2023 and August 2024 and consented to participation were included. Subjects with a global Clinical Dementia Rating (CDR) score of 0.5 were classified as MCI and subjects with a CDR score greater than or equal to 1.0 were classified as AD[51]. For subjects who did not have a CDR score available, the Montreal Cognitive Assessment (MoCA) score was used, where MCI was defined as a score between 18–25, and mild AD as a score between 10–17. All subjects in this cohort underwent a LF-MRI imaging protocol that included T1w, T2w and FLAIR sequences. The chronologically closest 1.5–3 T MRI acquired as standard of care was used for comparison and validation. A subset of patients (n = 7) returned for test-retest image acquisition using the aforementioned imaging protocol. CSF analysis was performed in patients who had CSF sampling and ADMark testing available (Athena, n = 21).

A subset of randomly selected participants from ADNI were used for validation of SynthSeg and WMH-SynthSeg on HF-MRI in those with AD/MCI compared with CN controls. Participants from ADNI-1 (N = 61; n = 32 males and n = 19 females) who underwent 1 mm isotropic T1 MP-RAGE image acquisition at 1.5 T were used for validation of morphometry using SynthSeg (Supplementary information Table S11). Dementia status was based on CDR scoring, where the CDR score for CN subjects was 0, for subjects with MCI the CDR was 0.5, and for subjects with AD it was 0.5–1. Full details on the parameters for image acquisition have been previously published[52]. For validation of WMH volume using WMH-SynthSeg, N = 58 randomly selected patients from ADNI-2 and ADNI-GO with a diagnosis of AD, MCI or CN who underwent HF-FLAIR acquisition were analyzed (Supplementary information Table S12). Details on the parameters for image acquisition have been reported previously[52].

Informed consent was obtained for all prospectively enrolled participants (cohorts 1, 3) or for secondary data analysis (cohort 2 and ADNI subgroups) under Mass General Brigham and/or Yale University Institutional Review Board approval. LF-MRI exclusion criteria included an inability to lay flat, body habitus exceeding the dimensions of the LF-scanner, pregnancy, or the presence of active electronic implants including a cardiac pacemaker, insulin pump, or spinal stimulator. Consent was obtained from the individual or their legally authorized representative.

Machine Learning Algorithms

The LF-SynthSR pipeline reported herein builds on our publicly available method, SynthSR[17,18,19]. The overall architecture used in training is summarized in Fig. 1a. As with SynthSR, LF-SynthSR relies on a synthetic data generator that creates batches of synthetic LF-MRI data with paired target outputs. The synthetic LF-MRI scans are produced from a pool of volumetric segmentations that have been pre-generated from a publicly available dataset of HF-MRI[53]. The target outputs include the aforementioned segmentations and corresponding 1 mm isotropic T1w scans. In LF-SynthSR v1, the generator used targeted simulation to create pairs of LF T1w- and T2w-like scans. In LF-SynthSR v2, the generator used domain-randomized simulation to create a single LF-like synthetic scan of random resolution and tissue contrast. This approach enables the trained network to process single scans of any contrast and resolution at test time[18].

LF-SynthSR uses the data from the synthetic generator to train a convolutional neural network (specifically a U-net)[54] with two losses: an image intensity loss and a segmentation loss[17,19]. The former compares the estimated high-resolution T1w scan with the ground truth (i.e., the authentic T1w scan acquired at HF) using the L1 norm, i.e., the sum of absolute differences in image intensities. The segmentation loss processes the estimated high-resolution T1w scan with a fully supervised U-net for image segmentation trained on real HF T1w scans, and compares the output with the ground truth segmentation. This loss encourages LF-SynthSR to produce image features that are well segmented, which is particularly helpful to penalize errors that have little impact on the L1 loss yet can noticeably degrade the segmentation, e.g., blurring of the putamen and claustrum[17,20].

At test time, the original v1 of LF-SynthSR used Robust Registration in the FreeSurfer environment[55] to align the anisotropic T1w and T2w LF-MRI scans from each healthy volunteer; registration is not required by v2 since it operates on individual scans. Both for v1 and v2, the resulting MP-RAGE-like images were each segmented with SynthSeg[20,56], which is publicly available, and which also relies on domain randomization to achieve high robustness.

For WMH-SynthSeg, the overall architecture of the training algorithm uses a similar generator as LF-SynthSR and SynthSeg, with two key differences[21]. First, the training data include scans with WMH (and corresponding segmentations), which we obtained from public datasets, including the Human Connectome Project, ADNI, and the WMH segmentation challenge[52,57–61]. This enables generation of synthetic images with WMH and corresponding ground truth segmentations with WMH masks. Second, WMH-SynthSeg achieves improved robustness with respect to SynthSeg, by solving three different tasks simultaneously (an approach known as "multi-task learning"): image segmentation; joint synthesis and super-resolution; and bias field estimation. This is in contrast with SynthSeg, which only predicts the segmentations. WMH-SynthSeg uses a multi-task U-net that simultaneously makes these three predictions; at test time, the bias field and synthetic T1w-like scan are discarded, and only the segmentation is preserved.

The full details of the training procedure have been previously reported[19–21], but are summarized here for completeness. The regression (LF-SynthSR) and segmentation networks (WMH-SynthSeg and the auxiliary segmentation network in LF-SynthSR) have the same architecture, except for the final layer: the regression networks have a linear layer with a single feature (the predicted intensities), whereas the segmentation U-Nets have as many features as labels to segment, followed by a softmax function. The U-nets are 3D and have five resolution levels with two layers each. These layers comprise convolutions with $3 \times 3 \times 3$ kernels followed by nonlinear activations using exponential linear units (ELU). The number of features is $24 \times 2^{(L-1)}$, where L = 1,…,5 is the level number. Training uses a large, fixed number of iterations that ensures convergence; we note that classical validation is not directly translatable to the domain randomization approach, since: (i) images are synthetic; and (ii) using real images in validation may skew the network towards their appearance (MRI contrast), potentially compromising the ability to analyze any MRI contrast and resolution.

Image analysis

All LF and HF dicom images were converted to NIfTI format prior to analysis with LF-SynthSR, SynthSeg, and/or WMH-SynthSeg for all cohorts. Ground truth was obtained by segmenting HF T1 MP-RAGE and/or FLAIR scans acquired at 1.5–3 T. HF T1 MP-RAGE images from healthy volunteers were additionally processed through the FreeSurfer segmentation pipeline ASEG[25]. Hippocampal, lateral ventricle, and whole brain volumes were compared between HF and LF counterparts. Quantitative metrics included agreement in segmentation volume (correlation and ASPD) and degree of spatial overlap (Dice similarity coefficient). For the hippocampus, the left and right volumes derived from the SynthSeg output for each subject were averaged. For ventricle volume, the left and right lateral ventricle volumes were combined. Whole brain volumes were computed by summing the following structures: cerebral white matter, cerebral cortex, thalamus, caudate, putamen, pallidum, hippocampus, ventral diencephalon, accumbens, and amygdala. Hippocampus, lateral ventricle and whole brain volumes were corrected for total intracranial volume to normalize/account for differences in head size. To compute the Dice, HF scans were co-registered to the super-resolved LF-MRI using a nonlinear approach with a grid spacing of 30 mm and computed kernel of 5 mm in NiftyReg and then both images were segmented using SynthSeg. HF images were co-registered to LF counterparts to preserve LF image resolution for downstream segmentation. However, LF co-registration to HF T1w MP-RAGE was also performed to determine the effect of co-registration direction on Dice scores. The equations for ASPD and Dice are listed below, where X corresponds to the segmentation volume of interest on the ground truth image at HF and Y corresponds to the segmentation volume of interest on the LF-MRI scan:

$$ASPD = 100\frac{|X - Y|}{(X+Y)/2} \quad (1)$$

$$Dice = 2\frac{|X \cap Y|}{|X| + |Y|} \quad (2)$$

To generate ground truth lesion volumes for WMH in cohort 2, the FLAIR sequences from the HF-FLAIR and LF-FLAIR were each manually segmented by consensus using ITK-Snap v3.8[62]. For each of the LF-MRI cohorts (1, 2 and 3), HF-MRI scans were acquired within 7 ± 11 months of the LF-MRI exam.

Statistical Analysis

Statistical analyzes were performed using STATA v18 (StataCorp, College Station, Texas, USA) and GraphPad Prism v10 (GraphPad Software, Boston, Massachusetts USA). Pearson correlations were performed with bootstrapping ($n = 400$ samples) to derive 95% confidence intervals. Comparisons between groups were evaluated using the Kruskal-Wallis test for more than 2 groups, and Wilcoxon rank sum test for 2 groups. A p-value < 0.05 was considered statistically significant.

Reporting summary

Further information on research design is available in the Nature Portfolio Reporting Summary linked to this article.

Data availability

Source data has been uploaded to the Harvard Dataverse repository (https://dataverse.harvard.edu) and is available via the following link: https://doi.org/10.7910/DVN/9PANMC. Individual patient data are available to academic researchers under restricted access due to privacy and ethical restrictions, and access can be obtained by contacting the corresponding author and entering into an institutional data use agreement.

Code availability

LF-SynthSR, SynthSeg and WMH-SynthSeg are publicly available and implemented in FreeSurfer: https://surfer.nmr.mgh.harvard.edu/fswiki/DownloadAndInstall. https://surfer.nmr.mgh.harvard.edu/fswiki/SynthSR. https://surfer.nmr.mgh.harvard.edu/fswiki/SynthSeg. https://surfer.nmr.mgh.harvard.edu/fswiki/WMH-SynthSeg.

References

1. 2023 Alzheimer's disease facts and figures. *Alzheimer's & Dementia* **19**, 1598–1695 (2023).
2. Gauthier, S., Webster, C., Servaes, S., Morais, J. & Rosa-Neto, P. *World Alzheimer Report 2022: Life After Diagnosis: Navigating Treatment, Care And Support*. (London, England, 2022).
3. Gauthier, S., Rosa-Neto, P., Morais, J. & Webster, C. *World Alzheimer Report 2021: Journey Through The Diagnosis Of Dementia*. (London, England, 2021).
4. Jack, C. R. et al. A/T/N: An unbiased descriptive classification scheme for Alzheimer disease biomarkers. *Neurology* **87**, 539–547 (2016).
5. Bateman, R. J. et al. Clinical and biomarker changes in dominantly inherited Alzheimer's disease. *N. Engl. J. Med* **367**, 795–804 (2012).
6. Cash, D. M. et al. The pattern of atrophy in familial Alzheimer disease: volumetric MRI results from the DIAN study. *Neurology* **81**, 1425–1433 (2013).
7. Kinnunen, K. M. et al. Presymptomatic atrophy in autosomal dominant Alzheimer's disease: a serial magnetic resonance imaging study. *Alzheimers Dement* **14**, 43–53 (2018).
8. Brickman, A. M. Contemplating Alzheimer's disease and the contribution of white matter hyperintensities. *Curr. Neurol. Neurosci. Rep.* **13**, 415 (2013).
9. Brickman, A. M. et al. Regional white matter hyperintensity volume, not hippocampal atrophy, predicts incident Alzheimer disease in the community. *Arch. Neurol.* **69**, 1621–1627 (2012).
10. Keret, O. et al. Pattern and degree of individual brain atrophy predicts dementia onset in dominantly inherited Alzheimer's disease. *Alzheimer's. Dement.: Diagnosis, Assess. Dis. Monit.* **13**, e12197 (2021).
11. McEvoy, L. K. et al. Alzheimer disease: quantitative structural neuroimaging for detection and prediction of clinical and structural changes in mild cognitive impairment. *Radiology* **251**, 195–205 (2009).
12. Kimberly, W. T. et al. Brain imaging with portable low-field MRI. *Nat. Reviews Bioengineering* 1,617–630(2023).
13. Zhao, Y. et al. Whole-body magnetic resonance imaging at 0.05 Tesla. *Science* **384**, eadm7168 (2024).
14. Mazurek, M. H. et al. Portable, bedside, low-field magnetic resonance imaging for evaluation of intracerebral hemorrhage. *Nat. Commun.* **12**, 5119 (2021).
15. Sheth, K. N. et al. Assessment of brain injury using portable, low-field magnetic resonance imaging at the bedside of critically ill patients. *JAMA Neurol.* **78**, 41 (2021).
16. Yuen, M. M. et al. Portable, low-field magnetic resonance imaging enables highly accessible and dynamic bedside evaluation of ischemic stroke. *Sci. Adv.* **8**, eabm3952 (2022).
17. Iglesias, J. E. et al. Quantitative brain morphometry of portable low-field-strength MRI using super-resolution machine learning. *Radiology* **306**, e220522 (2023).
18. Iglesias, J. E. et al. SynthSR: a public AI tool to turn heterogeneous clinical brain scans into high-resolution T1-weighted images for 3D morphometry. *Sci. Adv.* **9**, eadd3607 (2023).
19. Iglesias, J. E. et al. Joint super-resolution and synthesis of 1 mm isotropic MP-RAGE volumes from clinical MRI exams with scans of different orientation, resolution and contrast. *NeuroImage* **237**, 118206 (2021).

20. Billot, B. et al. SynthSeg: Segmentation of brain MRI scans of any contrast and resolution without retraining. *Med. Image Anal.* **86**, 102789 (2023).
21. Laso, P. et al. Quantifying white matter hyperintensity and brain volumes in heterogeneous clinical and low-field portable MRI. *Proc IEEE Int Symp Biomed Imaging*, 1–5 (2024).
22. Alves, F., Kalinowski, P. & Ayton, S. Accelerated brain volume loss caused by anti-β-amyloid drugs: a systematic review and meta-analysis. *Neurology* **100**, e2114–e2124 (2023).
23. Barkhof, F. & Knopman, D. S. Brain shrinkage in anti-β-amyloid Alzheimer trials: neurodegeneration or pseudoatrophy? *Neurology* **100**, 941–942 (2023).
24. Mulder, M. J., Keuken, M. C., Bazin, P.-L., Alkemade, A. & Forstmann, B. U. Size and shape matter: the impact of voxel geometry on the identification of small nuclei. *PLOS ONE* **14**, e0215382 (2019).
25. Fischl, B. et al. Whole brain segmentation: automated labeling of neuroanatomical structures in the human brain. *Neuron* **33**, 341–355 (2002).
26. Erten-Lyons, D. et al. Neuropathologic basis of white matter hyperintensity accumulation with advanced age. *Neurology* **81**, 977–983 (2013).
27. de Havenon, A. et al. Identification of white matter hyperintensities in routine emergency department visits using portable bedside magnetic resonance imaging. *J. Am. Heart Assoc.* **12**, e029242 (2023).
28. Fazekas, F., Chawluk, J. B., Alavi, A., Hurtig, H. I. & Zimmerman, R. A. MR signal abnormalities at 1.5 T in Alzheimer's dementia and normal aging. *AJR Am. J. Roentgenol.* **149**, 351–356 (1987).
29. Mattsson, N. et al. CSF biomarkers and incipient Alzheimer disease in patients with mild cognitive impairment. *JAMA* **302**, 385–393 (2009).
30. Hansson, O. et al. Association between CSF biomarkers and incipient Alzheimer's disease in patients with mild cognitive impairment: a follow-up study. *Lancet Neurol.* **5**, 228–234 (2006).
31. Ridha, B. H. et al. Volumetric MRI and cognitive measures in Alzheimer disease: comparison of markers of progression. *J. Neurol.* **255**, 567–574 (2008).
32. Sluimer, J. D. et al. Whole-brain atrophy rate and cognitive decline: longitudinal MR study of memory clinic patients. *Radiology* **248**, 590–598 (2008).
33. Dickerson, B. C. et al. MRI-derived entorhinal and hippocampal atrophy in incipient and very mild Alzheimer's disease. *Neurobiol. Aging* **22**, 747–754 (2001).
34. Chan, D. et al. Change in rates of cerebral atrophy over time in early-onset Alzheimer's disease: longitudinal MRI study. *Lancet* **362**, 1121–1122 (2003).
35. Schuff, N. et al. MRI of hippocampal volume loss in early Alzheimer's disease in relation to ApoE genotype and biomarkers. *Brain* **132**, 1067–1077 (2009).
36. Henneman, W. J. P. et al. Hippocampal atrophy rates in Alzheimer disease: added value over whole brain volume measures. *Neurology* **72**, 999–1007 (2009).
37. Johnson, K. A., Fox, N. C., Sperling, R. A. & Klunk, W. E. Brain imaging in Alzheimer disease. *Cold Spring Harb. Perspect. Med* **2**, a006213 (2012).
38. Leung, K. K. et al. Cerebral atrophy in mild cognitive impairment and Alzheimer disease: rates and acceleration. *Neurology* **80**, 648–654 (2013).
39. Nestor, S. M. et al. Ventricular enlargement as a possible measure of Alzheimer's disease progression validated using the Alzheimer's disease neuroimaging initiative database. *Brain* **131**, 2443–2454 (2008).
40. van Westen, D. et al. Cerebral white matter lesions - associations with Abeta isoforms and amyloid PET. *Sci. Rep.* **6**, 20709 (2016).
41. Pietroboni, A. M. et al. CSF beta-amyloid and white matter damage: a new perspective on Alzheimer's disease. *J. Neurol. Neurosurg. Psychiatry* **89**, 352–357 (2018).
42. Karvelas, N. & Elahi, F. M. White matter hyperintensities: complex predictor of complex outcomes. *J. Am. Heart Assoc.* **12**, e030351 (2023).
43. Marnane, M. et al. Periventricular hyperintensities are associated with elevated cerebral amyloid. *Neurology* **86**, 535–543 (2016).
44. Zhao, L., Luo, Y., Mok, V. & Shi, L. Automated brain volumetric measures with AccuBrain: version comparison in accuracy, reproducibility and application for diagnosis. *BMC Med Imaging* **22**, 117 (2022).
45. McNaughton, J. et al. Synthetic MRI generation from CT scans for stroke patients. *BioMedInformatics* **3**, 791–816 (2023).
46. O'Reilly, T., Teeuwisse, W. M., de Gans, D., Koolstra, K. & Webb, A. G. In vivo 3D brain and extremity MRI at 50 mT using a permanent magnet Halbach array. *Magn. Reson. Med.* **85**, 495–505 (2021).
47. Man, C. et al. Deep learning enabled fast 3D brain MRI at 0.055 tesla. *Sci. Adv.* **9**, eadi9327 (2023).
48. He, Y. et al. Use of 2.1 MHz MRI scanner for brain imaging and its preliminary results in stroke. *J. Magn. Reson.* **319**, 106829 (2020).
49. Cooley, C. Z. et al. A portable scanner for magnetic resonance imaging of the brain. *Nat. Biomed. Eng.* **5**, 229–239 (2021).
50. Liu, Y. et al. A low-cost and shielding-free ultra-low-field brain MRI scanner. *Nat. Commun.* **12**, 7238 (2021).
51. Trzepacz, P. T., Hochstetler, H., Wang, S., Walker, B. & Saykin, A. J. Relationship between the Montreal cognitive assessment and mini-mental state examination for assessment of mild cognitive impairment in older adults. *BMC Geriatrics* **15**, 107 (2015).
52. Jack, C. R. Jr. et al. The Alzheimer's disease neuroimaging initiative (ADNI): MRI methods. *J. Magn. Reson Imaging* **27**, 685–691 (2008).
53. Marcus, D. S. et al. Open access series of imaging studies (OASIS): cross-sectional MRI data in young, middle aged, nondemented, and demented older adults. *J. Cogn. Neurosci.* **19**, 1498–1507 (2007).
54. Ronneberger, O., Fischer, P. & Brox, T. U-Net: *Convolutional Networks for Biomedical Image Segmentation*. 234–241 (Springer International Publishing, Cham, 2015).
55. Reuter, M., Rosas, H. D. & Fischl, B. Highly accurate inverse consistent registration: A robust approach. *NeuroImage* **53**, 1181–1196 (2010).
56. Billot, B. et al. Robust machine learning segmentation for large-scale analysis of heterogeneous clinical brain MRI datasets. *Proc. Natl. Acad. Sci.* **120**, e2216399120 (2023).
57. Van Essen, D. C. et al. The WU-Minn human connectome project: an overview. *Neuroimage* **80**, 62–79 (2013).
58. Kuijf, H. J. et al. Standardized assessment of automatic segmentation of white matter hyperintensities and results of the WMH segmentation challenge. *IEEE Trans. Med Imaging* **38**, 2556–2568 (2019).
59. Carass, A. et al. Longitudinal multiple sclerosis lesion segmentation data resource. *Data Brief.* **12**, 346–350 (2017).
60. Commowick, O. et al. Objective evaluation of multiple sclerosis lesion segmentation using a data management and processing infrastructure. *Sci. Rep.* **8**, 13650 (2018).
61. Bellec, P. et al. The neuro bureau ADHD-200 preprocessed repository. *Neuroimage* **144**, 275–286 (2017).
62. Yushkevich, P. A. et al. User-guided 3D active contour segmentation of anatomical structures: significantly improved efficiency and reliability. *NeuroImage* **31**, 1116–1128 (2006).

Acknowledgements

This work was supported by the National Institutes of Health (EB031114, W.T.K., J.E.I., M.S.R. and K.N.S.), the Alzheimer's Association (24AARG-NTF-1187394, W.T.K.), the Fulbright Commission (A.J.S.-A.), and the American Heart Association-Tedy's Team postdoctoral fellowship award

(A.J.S.-A.). J.E.I. is funded by NIH BRAIN Initiative (RF1 MH123195, UM1 MH130981) and NIH grants (R01 AG07098 and RF1 AG080371). M.S.R. acknowledges the gracious support of the Kiyomi and Ed Baird MGH Research Scholar Award. All other co-authors report no relevant funding. Data used in preparation of this article were obtained from the Alzheimer's Disease Neuroimaging Initiative (ADNI) database (adni.loni.usc.edu). As such, the investigators within the ADNI contributed to the design and implementation of ADNI and/or provided data but did not participate in analysis or writing of this report. A complete listing of ADNI investigators can be found at: http://adni.loni.usc.edu/wp-content/uploads/how_to_apply/ADNI_Acknowledgement_List.pdf.

Author contributions

The senior corresponding author (Dr.W.T.K.) takes responsibility for all independent decisions made regarding study concept, analysis, and conclusions. Study design, data interpretation, and writing of the manuscript: A.J.S.-A., J.G., J.E.I., and W.T.K. Data analysis: A.J.S.-A., P.L., J.E.I., and W.T.K. Data acquisition: A.J.S.-A., J.G., J.K., J.Z., and K.N.S. Contributions and critical revision to the manuscript: J.E.I., J.K., J.Z., A.-L.G.G., P.S., S.P., Ad.H., M.S.R., K.N.S., and T.G.-I.

Competing interests

This study received research support from Hyperfine, Inc. (W.T.K. and K.N.S.). M.S.R. is a founder and equity holder of Hyperfine, Inc. Hyperfine had no role in the conceptualization, design, analysis, preparation of the manuscript, or decision to publish. M.S.R. has a financial interest in DeepSpin GmbH. His interests were reviewed and are managed by Massachusetts General Hospital, and Mass General Brigham in accordance with their conflict of interest policies.

Additional information

Supplementary information The online version contains supplementary material available at https://doi.org/10.1038/s41467-024-54972-x.

Correspondence and requests for materials should be addressed to W. Taylor Kimberly.

Peer review information *Nature Communications* thanks Ed Wu and the other, anonymous, reviewer(s) for their contribution to the peer review of this work. A peer review file is available.